

The position of the thermocouples in the foam was associated with an estimated uncertainty of ± 1 mm, whilst the error in the position in the aluminium heater block was neglected due to the high precision techniques used for its manufacture, and its high thermal conductivity. The voltage and current supplied to the cartridge heater were measured by a QM1323 and QM1571 multimeter, respectively. The manufacturer's specified accuracy for each multimeter in its respective measurement setting was $\pm (0.5\% + 2 \text{ dgt})$ and $\pm (2.5\% + 3 \text{ dgt})$. Current was monitored in real-time and sampled by the multimeter approximately every 30 s. The current was recorded throughout the 30 min measurement window once the temperature had stabilised. The standard deviation of the current data varied from 0.0042 to 0.012. The mean current supplied during this period was then calculated, along with its standard deviation to characterise the statistical component of its measurement uncertainty. The multimeter used to measure voltage did not feature PC connectivity, hence values were manually recorded every 15 s over a 5 min interval during the 30 min measurement window. Voltage was observed to be much more stable than current, with a standard deviation that remained below 0.005 across all tests. Standard error accounting was conducted for all calculated, experimental values in this work, as in [28]. Systematic and standard errors were combined and reported in the form of a 95% confidence interval where appropriate.

3.3. Heat loss analysis

Heat loss in published natural convection studies is typically estimated using Fourier's law of conduction in one dimension, which is not strictly applicable in this case due to the extended geometry of the heater block. Heat loss was expected to occur through all six sides of the assembly, primarily from the top face and the upper portions of the four vertical sides, and to a lesser extent through the base. To estimate heat loss, and allow calculation of the heat sink thermal resistance, the entire experimental rig was modelled numerically. Once close agreement between the modelled and experimentally measured heat sink base temperature was achieved, a numerical estimate of the heat loss could be made with confidence.

4. Numerical model

4.1. Model validation

4.1.1. Modelling methodology

The commercial heat sink outlined in Section 3.1 was adopted to develop a robust, validated numerical model of heat sink performance. A three-dimensional, transient *COMSOL Multiphysics* model comprising the experimental setup, including the full test apparatus and surrounding air, was used to solve the momentum and energy equations of the system. Physics settings, mesh resolution, and solver settings were refined using this model, which was then adapted for parametric studies using newly proposed geometries. For all numerical models described herein, a five hour transient simulation was used, with data output at 15 min intervals for analysis. Final values at the end of the five hour computational period were taken as the steady state values. Surface roughness effects were neglected throughout, with the expectation that the rougher surfaces resulting from a 3D printed heat sink may compensate for the reduced thermal conductivity of the 3D printed aluminium alloy [2]. Further information about the model is provided below.

4.1.2. Computational domain

The computational domain consisted of a quarter segment with overall dimensions $1.5 \text{ m} \times 1 \text{ m} \times 1 \text{ m}$ (Figs. 4 and 5), that utilises two vertical symmetry planes. Whilst the overall size of the fluid domain was smaller than the size of the test chamber, increasing the domain further did not lead to any appreciable changes in the model results. Furthermore, taking the full size of the chamber for the fluid domain

would introduce difficulties in selecting appropriate boundary conditions for the model. The solid domains reflect the physical dimensions outlined in Section 3, and includes the 5.5 mm diameter, 4 mm tall head from the cap screws used to fix the heat sink to the test platform.

4.1.3. Fluid physics boundary conditions

The fluid flow boundary conditions for the fluid domain in the model were set as follows. The base of the fluid domain, and all the fluid-solid boundaries, were set as a wall with a no-slip condition. The two vertical, far walls were set as open boundaries with a zero normal stress boundary condition, imposing $p \approx f_0 = 0 \text{ N}\cdot\text{m}^{-2}$, where f_0 is the boundary stress vector directed in a negative normal orientation. The top of the fluid domain was set as a constant pressure outlet boundary condition ($p_0 = 0 \text{ Pa}$), with backflow suppression. The remaining two near walls were set as symmetry boundaries. Gravity was applied throughout the domain in the negative z -direction to allow for buoyancy driven flow. Fluid flow overall was modelled as laminar and fully compressible.

4.1.4. Heat transfer physics boundary conditions

The heat transfer boundary conditions for the entire model (comprising the fluid and solid domains) were set as follows. The heat sink, heater block, and insulation were modelled as solid bodies using the heat equation and the thermophysical properties described earlier. The base of the domain was set as an adiabatic boundary. Again the two far fluid boundaries were modelled as open boundaries, which in this context are described using Eqs. (4) and (5) below. Since air was expected to be entering the computational domain through these boundaries, they were effectively isothermal at the ambient temperature T_a .

$$T = T_a, \quad \text{if } \mathbf{n} \cdot \mathbf{u} < 0 \quad (4)$$

$$-\mathbf{n} \cdot \mathbf{u} = 0, \quad \text{if } \mathbf{n} \cdot \mathbf{u} \geq 0 \quad (5)$$

Heat was introduced to the system through a volume source term in

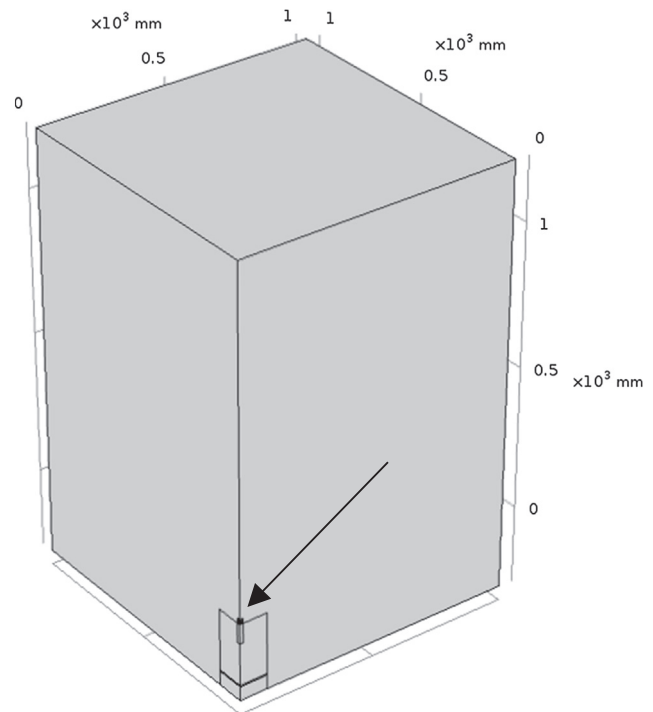


Fig. 4. Computational domain used for grid refinement and validation studies. Includes insulation, heater block, fluid domain, and heat sink. Quarter segment shown utilising plane symmetry. The arrow indicates the position of the heat sink domain.

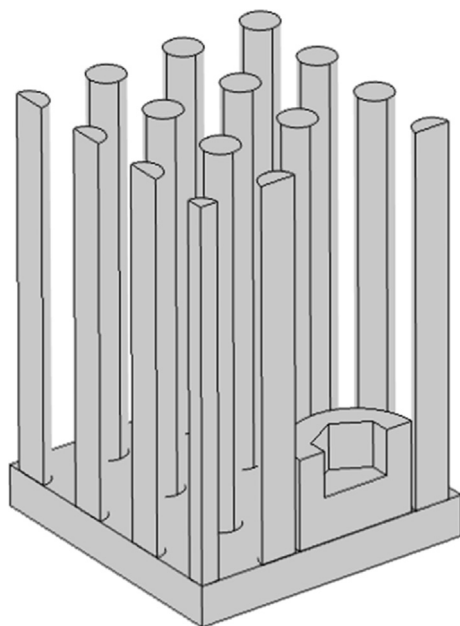


Fig. 5. Heat sink domain from Fig. 4 showing pin configuration and the modelled M4 cap screw head.

the heater block ($\dot{Q} = \dot{Q}_0 = P_0/V$), where \dot{Q} is the source term, \dot{Q}_0 is the volumetric heat rate, P_0 is the supplied heating power, and V is the heater block domain volume.

The supplied thermal energy was conducted to the heat sink and the surrounding foam insulation, and then to the surrounding air. The heater block was assumed to be in perfect thermal contact with the surrounding foam and the heat sink. The temperature difference measured experimentally between the heat sink base and the upper surface of the heater block was smaller than the uncertainty of the measurement, supporting the assumption of negligible thermal contact resistance between these bodies.

4.1.5. Surface-to-surface radiation and heat sink emissivity

Early experimental investigations of natural convection pin-fins by Sparrow and Vemuri [10,11] established the strong contribution of radiative loss to the overall heat exchange under natural convection conditions [10,11,29], which tends to increase with pin-fin array density and height [8]. Various experimental studies of pin fins heat sinks have reported radiation heat loss representing 19–48% [30], 34–48% [31], 25–40% [11] and 25–45% [10] of the total heat exchange with the surroundings. These results suggest that radiative heat loss is a critical component of natural convection heat sink performance [4,10,11,30,31], particularly for sparsely populated pin fin arrays, and must therefore be considered in the current numerical model. As such the heat sink wetted surfaces were set to participate in surface-to-surface radiation exchange. This was achieved by using the direct area integration method in *COMSOL Multiphysics*, which ignores shadowing effects for concave surfaces to enhance computational speed and accuracy for simple geometries, such as the cylinders and pins seen on conventional heat sinks. A brief description of the radiation model is provided below.

The radiative heat flux term \dot{q}_r for an ideal greybody is given by Eq. (6) below, where G is the irradiance (radiation heat flux arriving at the surface) and E_b is the temperature dependent total blackbody emissive power (radiation heat flux leaving the surface) [32].

$$\dot{q}_r = \varepsilon(G - E_b) \quad (6)$$

The irradiation (G) for the current model comprises radiation arriving on the surface element from other adjacent boundaries in the model only, since there is no ambient or external radiation source

defined. To calculate this irradiation term, the model must account for all the participating surfaces in the field of view of a given surface element, which is represented by the view factor [33]. A detailed derivation of the view factor is provided elsewhere [32–35]. The radiative heat flux term (\dot{q}_r) was then added to the governing energy equation for heat transfer in fluids (Eq. (7)) used in *COMSOL*, taken from [36].

$$\rho C_p \left(\frac{\partial T}{\partial t} + \mathbf{u} \cdot \nabla T \right) + \nabla \cdot (\dot{q}_{cd} + \dot{q}_r) = \dot{Q}_p + \dot{Q}_{vd} + \dot{Q}_s \quad (7)$$

Here, \mathbf{u} is the velocity vector, \dot{q}_{cd} is the conduction heat flux, \dot{q}_r is the radiation heat flux, \dot{Q}_p is the pressure-work term, \dot{Q}_{vd} is the viscous dissipation term, \dot{Q}_s is the additional heat source term, and the gradient and divergence operators are represented by their typical symbols.

For the external surfaces of the foam insulation, no difference was observed when radiation was included on its external surface boundaries, so it was excluded from the model to conserve computational resources.

The emissivity of the commercial heat sink was estimated by the method outlined in [14], using a FLIR X6540sc thermal imaging camera. A Type T, Class 1 thermocouple was inserted into the heat sink base at ambient temperature. Once its temperature stabilised, the emissivity setting was varied on the IR camera software in increments of 0.05. The surface temperature was recorded at each emissivity setting across a variety of points on the heat sink. The data were then compiled and linear interpolation was used to estimate the emissivity value that matches the thermocouple temperature with the observed temperature by the IR camera. The emissivity value was found to be approximately 0.92 at 22.5 °C. The external boundaries of the air domain were set as transparent to radiation. The built-in material properties for air, aluminium, and acrylic were used for the air domain, heat sink domain, and thin acrylic base slab, respectively.

4.1.6. Mesh refinement

The key metric used to assess grid convergence was the volume averaged temperature of the heat sink base. This was selected because the base temperature is easy to measure experimentally and is not expected to show significant spatial variation. An unstructured, non-uniform mesh with extensive refinement in the fluid region surrounding the heat sink was created with 368,143 elements (mesh 1). A detailed, close-up view of mesh 1 is shown in Fig. 6, which highlights the high resolution elements used in the fluid region surrounding the heat sink. The results from this mesh were compared against a much finer mesh with 1,160,038 elements (mesh 2). The average heat sink base temperature was found to be 55.3 °C and 55.4 °C for mesh 1 and mesh 2, respectively.

Mesh independence was assessed using both the relative error (ϵ_{ij}), and the grid convergence index (GCI_{ij}) as outlined by Roache [37], which were 0.2% and 1.3%, respectively. Given the small variation between the two meshes and significant computational demand for the finer mesh, the mesh with 368 143 elements was deemed sufficient for this study.

4.2. Parametric design study for heat sink performance enhancement

For the parametric design study, the heater block and insulation were removed from the computational domain, leaving only the heat sink body, and fluid domain that was kept at its original dimensions. A constant heat rate boundary condition was imposed at the base of the heat sink equal to 2.15 W, allowing a direct comparison of different designs. Minor adjustments were made to the mesh, as required by the various heat sink geometries, so as to ensure consistency between studies, and to enhance solution time. In all cases, the number of mesh elements was kept between approximately 322,000 and 447,000. All studies were conducted with the power input and ambient temperature given in Section 2.